

Contents lists available at ScienceDirect

Journal of Catalysis

journal homepage: www.elsevier.com/locate/jcat



Catalyst consisting of Ag nanoparticles anchored on amine-derivatized mesoporous silica nanospheres for the selective hydrogenation of dimethyl oxalate to methyl glycolate



Guilin Dong ^{a,1}, Yueqiang Cao ^{b,1}, Sainan Zheng ^c, Jinghong Zhou ^{b,*}, Wei Li ^a, Francisco Zaera ^{d,*}, Xinggui Zhou ^b

- ^a School of Chemical Engineering, East China University of Science and Technology, 130 Meilong Road, Shanghai 200237, China
- ^b State Key Laboratory of Chemical Engineering, East China University of Science and Technology, 130 Meilong Road, Shanghai 200237, China
- ^c Pujing Chemical Industry Co.,Ltd., 166 Minhong Road, Shanghai 201102, China
- ^d Department of Chemistry and UCR Center for Catalysis, University of California, Riverside, CA 92521, United States

ARTICLE INFO

Article history: Received 13 July 2020 Revised 10 August 2020 Accepted 11 August 2020 Available online 25 August 2020

Keywords: DMO hydrogenation Methyl glycolate Surface amination Confinement Silver catalyst

ABSTRACT

Developing efficient catalysts for the selective hydrogenation of dimethyl oxalate (DMO) is of great significance for the coal-based production of methyl glycolate (MG), but designing processes for this conversion is challenging. Herein we report an unprecedented catalytic performance for the selective hydrogenation of DMO to MG, achieved by using a catalyst based on Ag nanoparticles anchored inside the mesopores of amine-derivatized silica nanospheres (NH₂-MSNS). It was determined that the unique microenvironment endowed by the amine-derivatized channel surfaces helps this Ag catalyst promote the activation of DMO and H₂ to yield MG with high selectivity, and also prevents sintering and coking, hence improving stability. Accordingly, the resulting Ag/NH₂-MSNS catalyst was shown to be capable of promoting the hydrogenation reaction with a turnover frequency of 230 h⁻¹ and a MG selectivity of 97% at nearly 100% of DMO conversion, a performance that was sustained for at least 250 h; these results are significantly better than those seen with other reported catalysts. Our study points to a promising route for the development of high-performing Ag catalysts to be used in the coal-based MG production.

© 2020 Elsevier Inc. All rights reserved.

1. Introduction

The catalytic selective hydrogenation of dimethyl oxalate (DMO), a product from coal-based syngas, has been shown to be a promising and eco-friendly route to methyl glycolate (MG), an important fine chemical intermediate for pharmaceuticals, perfumes and polymers production [1–7]. Ag-based catalysts have been reported hitherto as the most efficient for this reaction because of their relatively weak hydrogenolysis activity (hydrogenolysis leads to the formation of undesirable byproducts), and also because of their low activity for the over-hydrogenation of MG [8,9]. Moreover, it has been shown that the nature of the Ag-based catalysts often dictates their hydrogenation activity. Most Ag-based catalysts show low activity, a problem that is usually addressed by employing high metal loadings [10–15]. However, that increases the catalyst cost, lowering its industrial

applicability, and favors the sintering of the dispersed Ag nanopar-

Herein, we report that anchoring Ag nanoparticles onto the surface of mesoporous silica nanospheres functionalized by an (amine-based) electron-donor group can significantly boost their catalytic activity and stability for the selective hydrogenation of DMO to MG. As explained in more detail below, we believe that the unique performance seen with our catalyst may be due to the high dispersion achieved for the Ag nanoparticles thanks to both the use of mesoporous materials and the derivatization of the silica surface prior to the metal deposition in order to provide appropriate nucleation centers. The resulting sample contains Ag

ticles at high reaction temperatures, thus degrading both the Ag utilization efficiency and catalytic stability. There is also the issue of the electronic structure of the metal: previous reports indicate that electron-rich Ag nanoparticles promote the activation of both hydrogen and the DMO reactant, and thus enhance hydrogenation activity [16,17]. Therefore, an efficient strategy is required for the precise tuning of the physiochemical environment of Ag catalysts in order to optimize their performance.

^{*} Corresponding authors.

E-mail addresses: jhzhou@ecust.edu.cn (J. Zhou), zaera@ucr.edu.cn (F. Zaera).

¹ These authors contributed equally to this work.

nanoparticles significantly smaller and more resistant toward sintering than those seen in previous catalysts.

2. Experimental

2.1. Chemicals

Cetyltrimethylammonium chloride (CTAC), triethanolamine (TEA), and 3-aminopropyltrimethoxysilane (APTS) were purchased from J&K Scientific Ltd. Tetraethyl orthosilicate (TEOS), cyclohexane, methylbenzene, ethanol, and silver nitrate (AgNO₃) were purchased from Sinopharm Chemical Reagent Co., Ltd. All the reagents were used as received without further purification.

2.2. Preparation of the MSNS support

The MSNS was synthesized via a biphasic stratification approach using TEOS as the silica source and CTAC as the template agent, according to a method reported in the literature [18]. Typically, 15 g of CTAC was first dissolved in 120 mL of deionized water, after which 0.4 g of TEA was added. The mixture was stirred gently at 333 K for 1 h. Subsequently, a solution of 7.5 g of TEOS in 25 g of cyclohexane was added drop-wise to the water-CTAC-TEA mixture, which was then stirred continuously at 333 K for 12 h. The resulting mixture was collected by centrifugation and washed with ethanol to remove the residual reactants. After drying at 393 K for 4 h, the CTAC-templated MSNS solid (denoted as Sur-MSNS) was obtained. Finally, the Sur-MSNS was calcined at 823 K for 4 h in static air to remove the template and obtain the desired MSNS support.

The amino-functionalized MSNS (NH₂-MSNS) was synthesized by silanization of APTS via a post-grafting strategy [19]. Typically, 1.5 g of MSNS was dispersed in 50 g of toluene to form a homogeneous suspension, and then 0.5 g of APTS was added. The mixture was refluxed at 383 K for 12 h, after which it was centrifugated and washed with ethanol to remove the residual reactants. After drying at 393 K for 4 h, the amino-functionalized MSNS (denoted as NH₂-MSNS) was obtained.

2.3. Preparation of Ag/MSNS and Ag/NH₂-MSNS catalysts

The MSNS and NH_2 -MSNS supported Ag catalysts were prepared via in situ reduction of Ag salts. Typically, 1.0 g of MSNS/ NH_2 -MSNS was dispersed in 90 mL of ethanol by sonication to form a uniformly dispersed suspension. After the mixture was stirred for 30 min at 303 K, 0.049 g of $AgNO_3$ in 24.5 mL of ethanol was added drop-wise and stirred at the same temperature for 4 h. Then the temperature was increased to 343 K, and the mixture was stirred for 24 h until the color of the suspension changed into brown. After centrifugation, the product was washed with ethanol and dried at 333 K for 12 h under a nitrogen atmosphere to obtain the corresponding Ag/MSNS or Ag/NH_2 -MSNS catalyst.

2.4. Catalyst characterizations

Fourier-transform infrared (FTIR) spectra were recorded in the $400-4000~{\rm cm^{-1}}$ range on a Nicolet 6700 spectrometer equipped with a deuterium tri-glycine sulfate (DTGS) detector. The powder samples were mixed with KBr (2 wt%) and pressed into translucent disks at room temperature. The N₂ adsorption–desorption isotherms of the catalysts were measured at 77 K using a Micrometrics ASAP 2020 apparatus. The samples were degassed at 573 K for 3 h to remove physically-adsorbed impurities prior to the measurements. The specific surface areas (S_{BET}) were calculated according to the Brunauer–Emmett–Teller (BET) method. The aver-

age pore diameters and pore size distributions were obtained by analyzing the desorption branch of the isotherms using the Barret-Joyner-Halenda method.

Transmission electron microscopy (TEM) images were obtained on a JEOL JEM-2100F instrument with an operating voltage of 200 kV. The high-angle annular dark-field scanning transmission electron microscopy (HAADF-STEM) images were acquired on a FEI Tecnai G2 F20 S-Twin instrument with an operating voltage of 200 kV. The actual loading of silver in the catalysts was determined by ion-coupled plasma optical emission spectroscopy (ICP-OES) using an Agilent 5100 spectrometer. The actual content of nitrogen in the samples was estimated by using an Elementar Vario ELIII elemental analyzer. The powdered X-ray diffraction (XRD) patterns of the samples were collected on a Bruker D8 Advance X-ray diffractometer in the scanning angle (2θ) range of 10° to 80° at a scanning speed of 2° min $^{-1}$ using nickel-filtered Cu K α radiation (λ = 1.5418 Å). UV-visible diffuse reflectance spectra (UV-vis DRS) were recorded in the 200-800 nm range on an Agilent CARY 5000 UV-vis-NIR scanning spectrophotometer with an integrating attachment using BaSO₄ as the background standard. X-ray photoelectron spectroscopy (XPS) was carried out on a Thermo Fisher K-Alpha spectrometer equipped with an Al K α Xray radiation source (hv = 1486.6 eV) and a multichannel detector. A flood gun with variable electron accelerating voltages (from 6 to 8 eV) was used for charge compensation. The binding energies were calibrated in reference to a value of BE = 284.6 eV for the carbonaceous C 1s XPS signal.

The N₂O chemisorption, H₂ temperature-programmed reduction (H2-TPR), and H2, DMO, and CO2 temperature-programmed desorption (H₂-TPD, DMO-TPD, CO₂-TPD respectively) experiments were carried out in a Micrometrics Autochem II 2920 apparatus with a thermal conductivity detector (TCD). For N₂O chemisorption, 100 mg of the solid sample was first reduced at 623 K under a flow of 50 mL·min⁻¹ of 10% H₂/Ar for 3 h and then cooled down to 363 K. Subsequently, the sample was exposed to the pure N₂O (30 mL·min⁻¹) for 1 h to ensure that the surface metallic silver atoms were completely oxidized to Ag₂O. The sample was purged with a flow of Ar (30 mL·min⁻¹) for 30 min and then cooled down to room temperature under Ar atmosphere. Next, 10% H₂/Ar (50 mL·min⁻¹) was introduced, and the sample was heated up to 1073 K at rate of 10 K·min⁻¹, during which the hydrogen consumption was monitored using the TCD [20]. In a typical procedure for the TPD tests, 100 mg of sample was reduced at 623 K for 3 h in a 10% H₂/Ar atmosphere, followed by purging with He for 2 h at 573 K to remove physically adsorbed impurities. After cooling the sample down to 323 K, a flow of the probe molecule (H2 for H₂-TPD, DMO for DMO-TPD, and CO₂ for CO₂-TPD; for the DMO-TPD experiments the vapor of DMO was carried by Ar) was started until saturated adsorption was reached. The probe molecule was then removed by purging with Ar until the baseline of the MS signal was stabilized. After cooling to room temperature, the TPD profile was collected in Ar from room temperature to 1073 K at a ramping rate of 5 K·min⁻¹. The desorbed probe molecule was monitored by using an online mass spectrometer (MS).

In situ FTIR spectra of DMO adsorbed on the catalysts were recorded using a Perkin-Elmer Frontier spectrometer and a transmission FTIR cell. Briefly, 30 mg of dried catalyst was compressed into a self-supporting wafer and carefully loaded into the transmission cell. The catalyst was reduced at 623 K under $5\%\,H_2/N_2$ for 3 h and then evacuated by N_2 for 30 min to remove the chemisorbed hydrogen. After cooling down to 353 K, DMO was evaporated and flowed through the cell with the aid of a vacuum pump for 1 h. That was followed by evacuation to remove any weakly-adsorbed DMO. The FTIR spectra were then recorded at the reaction temperature (i.e., 493 K) with a spectral resolution of 4 cm $^{-1}$ and via the accumulation of 64 scans.

2.5. Catalytic evaluation

The catalytic performance of the solid samples for the promotion of the vapor-phase hydrogenation of DMO was carried out in a stainless steel fixed-bed tubular flow reactor equipped with a computer-controlled auto-sampling system. Typically, 350 mg of the catalyst (40-60 mesh) was loaded into the center of the reactor, and both sides of the catalyst bed were packed with quartz powder (40-60 mesh). Prior to catalytic performance evaluation, the catalyst was reduced under a H₂ flow of 30 mL·min⁻¹ at 623 K for 4 h. After cooling to the reaction temperature of 493 K, a 10 wt% DMO in methanol solution was pumped into the catalyst bed with a P230 digital HPLC pump (eliteHPLC) at a H₂/DMO molar ratio of 80 and a system pressure of 2.0 MPa. The outlet stream was sampled at intervals of 30 min using an automatic Valco 6-port valve system and analyzed using an online gas chromatograph (Agilent 7890A) equipped with flame ionization detection and a KB-Wax capillary column (30 m \times 0.45 mm \times 0.85 μ m).

The conversion of DMO and the selectivity toward each product were calculated based on the following equations:

Conversion (%) =
$$\frac{mol\ of\ DMO\ (in) - mol\ of\ DMO(out)}{mol\ of\ DMO(in)} \times 100\%$$

$$Selectivity~(\%) = \frac{\textit{mol of MG or EG (out)}}{\textit{mol of DMO (in)} - \textit{mol of DMO (out)}} \times 100\%$$

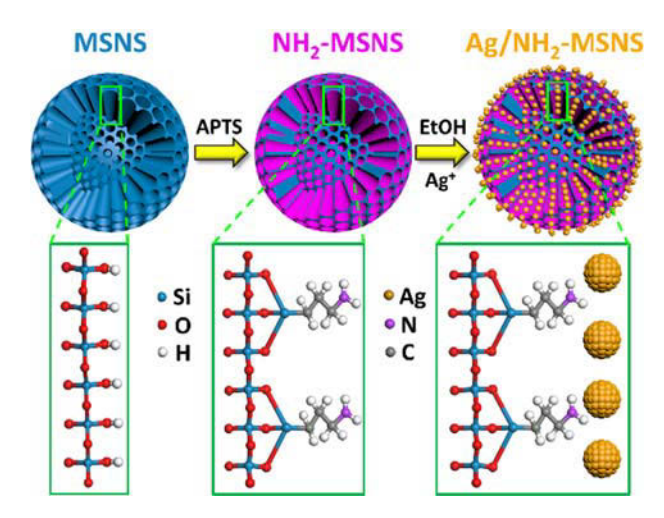
Turnover frequencies (TOF) were calculated according to the following equation [21]:

$$TOF = \frac{W \times V \times C_{DMO}}{D \times N_{Ag}}$$

where W is the DMO concentration in the DMO/methanol solution (mol/L), V is the flow rate of the DMO/methanol solution (L/h), C_{DMO} is the DMO conversion, N_{Ag} is the total amount of Ag (mol) in the used catalyst and D is the Ag dispersion obtained from N_2O chemisorption and H_2 -TPR measurements. For the TOF measurements, the reaction was performed at 5.0 and 12.0 h^{-1} LHSVs for Ag/MSNS and Ag/NH₂-MSNS, respectively, while the other reaction conditions were kept the same (T = 493 K, P = 2.0 MPa and H_2 /DMO = 80). This was necessary to ensure that the conversion of DMO was below 20% (they were 18.8% and 19.3%, respectively).

3. Results & discussion

Our catalysts were built on mesoporous silica nanospheres (MSNS) by following the synthetic steps depicted in Scheme 1. The MSNS were synthesized via a biphasic stratification approach using tetraethyl orthosilicate (TEOS) as a silica source and cetyltrimethylammonium chloride as a template agent [18], and their surfaces were then modified via silanization with 3aminopropyl-trimethoxysilane (APTS) to enhance the anchoring of the Ag precursor (AgNO₃) [19]. Fig. 1a and b show TEM images of the as-synthesized MSNS and the material obtained after amination (NH2-MSNS), respectively. Similarly sized nanospheres with center-radial mesopores are evident in the images of both samples, indicating that the surface amination step does not change the morphology of the MSNS. N₂ physisorption measurements (Fig. S1 and Table 1) point to decreases in pore size, pore volume, and specific surface area upon amination, an expected as a consequence of the grafting of the ATPS onto the surface of the mesoporous channels of MSNS. In addition, the FTIR difference spectrum between the MSNS and NH₂-MSNS samples (Fig. 1c) clearly shows absorption bands at 1562 and 700 cm⁻¹, corresponding to NH deformation modes [22], and at 2924, 2850 and



Scheme 1. Main steps in the preparation of our catalysts: Surface amination of MSNS is followed by immobilization of Ag NPs onto the aminated MSNS.

1460 cm⁻¹, associated with CH₂ vibrations [23]; those are all assignable to the propylamine surface moieties added by amination (individual spectra for each sample are reported in Fig. S2). The XPS spectrum of NH₂-MSNS in Fig. 1d shows a prominent N 1s peak absent in the trace from the pristine MSNS. All these results strongly point to the successful surface amination of the mesoporous silica nanospheres.

The next step in our catalyst preparation was the addition of Ag nanoparticles to the NH₂-MSNS amine-derivatized support. The solid was exposed to a solution of a Ag salt (AgNO₃) to create metal nucleation sites inside the mesopores via the interaction between the surface amino group and the precursor. The immobilized Ag precursor was then reduced with ethanol to grow the Ag nanoparticles and produce the Ag catalyst. The HAADF-STEM images of the resulting Ag/NH₂-MSNS catalyst, together with those of a Ag/MSNS reference catalyst (where Ag was deposited on the underivatized and pristine surface of MSNS), are shown in Fig. 1e and f, respectively, and the corresponding TEM images are reported in Fig. S3. Uniformly dispersed Ag nanoparticles, with average diameters of approximately 5.5 nm, are clearly observed in the Ag/NH₂-MSNS catalyst, whereas a broader distribution of Ag nanoparticles ranging from 1 to 12 nm in diameter are evident in the images for the Ag/MSNS catalyst. Notably, in the NH₂-MSNS support, the Ag nanoparticles are predominantly located inside its mesopores, whereas in the case of the Ag/MSNS sample some nanoparticles are quite large and must be located on the outside.

The small size of the Ag nanoparticles in NH₂-MSNS is also evidenced by the lack of discernable diffraction lines for Ag in the XRD pattern for the Ag/NH₂-MSNS catalyst; in contrast, those are clearly seen for Ag/MSNS (Fig. S4) [24]. In addition, the UV-vis spectrum of the Ag/NH₂-MSNS catalyst (Fig. S5) shows a blue-shifted surface plasmon resonance peak in comparison with that of the Ag/MSNS catalyst, indicative of the smaller size of the Ag nanoparticles in NH2-MSNS case [25-27]. Results from N2O chemisorption and H₂-TPR experiments (Table 1) highlight the higher Ag dispersion and specific Ag surface area in the Ag/NH2-MSNS catalyst compared to those in the Ag/MSNS sample, an expected consequence from the smaller nanoparticles sizes seen in the former catalyst. The average Ag particle size of Ag/NH₂-MSNS, estimated from the measured dispersion (Table S1), is smaller than that of Ag/MSNS, which agrees well with the results from the abovementioned TEM and HAADF-STEM characterizations. All these results also clearly show that the smaller Ag nanoparticles are more homogeneously immobilized inside the mesopores of NH2-MSNS than in

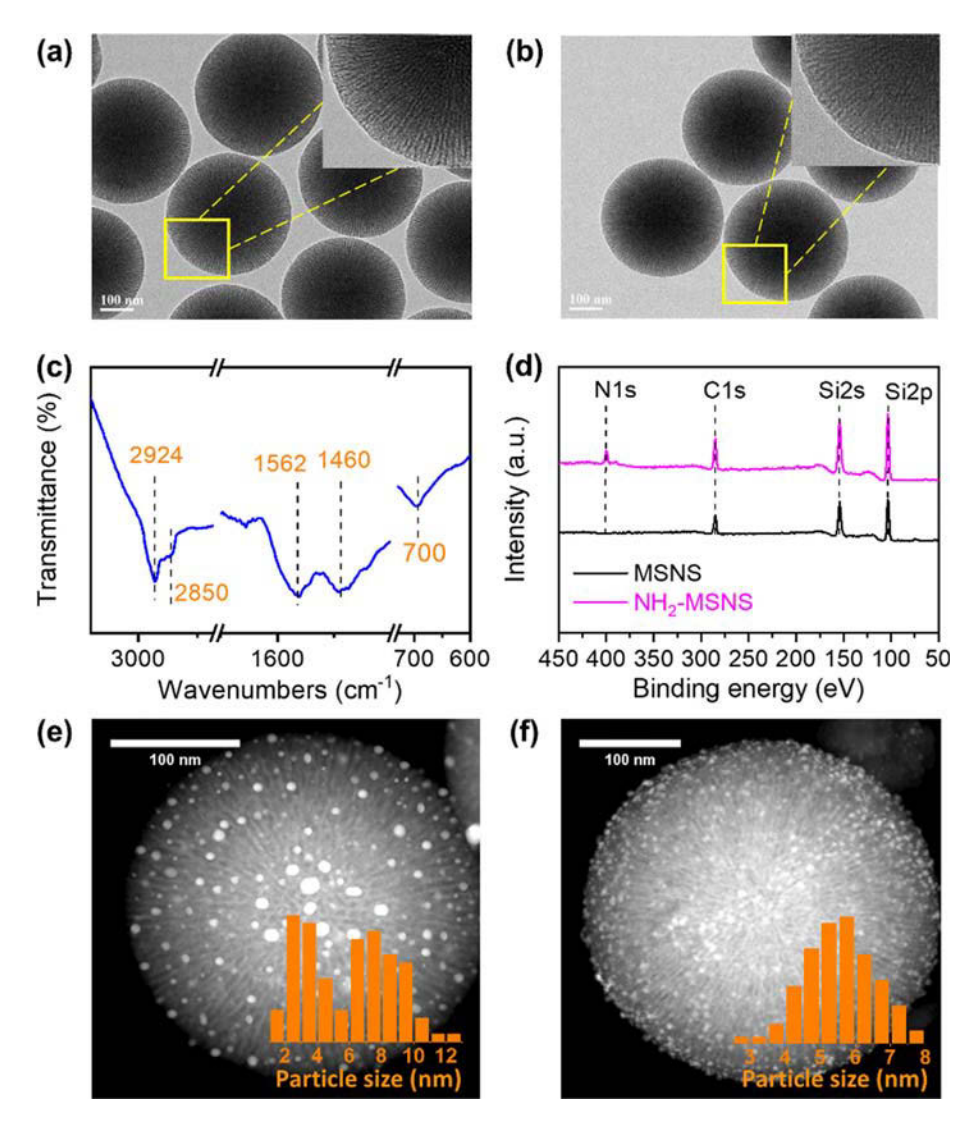


Fig. 1. TEM images of (a) MSNS and (b) NH₂-MSNS. The insets provide enlarged views of the area marked by the yellow squares. (c) Difference FTIR spectrum obtained by subtracting the FTIR spectrum of MSNS from that of NH2-MSNS. (d) XPS spectra of MSNS and NH2-MSNS. (e, f) HAADF-STEM images of the (e) Ag/MSNS and (f) Ag/NH2-MSNS catalysts. The insets are the corresponding histograms of the particle size distributions.

Physicochemical properties of the different supports and catalysts from this study.

Sample	MSNS	NH ₂ -MSNS	Ag/MSNS	Ag/NH ₂ -MSNS	
Ag content ^[a] (wt%)	_	_	2.5	2.9	
N content ^[b] (wt%)	_	2.28	_	2.19	
$S_{BET}^{[c]} (m^2 g^{-1})$	665	323	390	242	
$V_{pore}^{[d]}(m^{3}g^{-1})$	0.80	0.41	0.54	0.33	
D _{pore} [e] (nm)	6.61	6.17	6.39	6.12	
$d_{Ag \cdot TEM}^{[f]}$ (nm)	_	_	6.6 ± 2.7	5.5 ± 0.9	
Dispersion ^[g] (%)	_	_	20.8	31.7	
$S_{Ag}^{[g]}(m_{\cdot}^{2}g^{-1})$	_	_	2.52	4.46	
$TOF(h^{-1})$	_	_	165.1 ^[h]	230.1 ^[i]	

[[]a] Determined by ICP-OES.

[[]b] Determined using an element analyzer.

[[]c] Specific surface area, calculated by the BET method.

[[]d] BJH adsorption cumulative pore volume.

[[]e] BJH adsorption average pore diameter.

[[]f] Average size of Ag nanoparticles determined by TEM.

[[]g] Dispersion and surface area of Ag (SAg) obtained from N2O chemisorption and H2-TPR measurements. The detailed calculations are shown in the Supplementary Information.

[[]h] Based on a 18.8% DMO conversion under the following reaction condition: T = 493 K, P = 2.0 MPa, $H_2/\text{DMO} = 80 \text{ and LHSV} = 5.0 \text{ h}^{-1}$. [i] Based on a 19.3% DMO conversion under the following reaction condition: T = 493 K, P = 2.0 MPa, $H_2/\text{DMO} = 80 \text{ and LHSV} = 12.0 \text{ h}^{-1}$.

the reference untreated MSNS, a difference that we believe accounts for the better anti-sintering and catalytic performance seen here for the DMO hydrogenation to MG (see below).

The electronic properties of the Ag/NH2-MSNS catalyst were subsequently probed by X-ray photoelectron spectroscopy (XPS). Fig. 2 shows the Ag 3d XPS data obtained for both Ag/NH₂-MSNS and Ag/MSNS catalysts as well as the N 1s XPS traces for Ag/ NH₂-MSNS and the original NH₂-MSNS support. The N 1s XPS spectrum of the NH2-MSNS support exhibits two peaks at 398.9 and 401.0 eV corresponding to -NH₂ and -NH₃ species, respectively [28,29]. After immobilization of the Ag nanoparticles these peaks shift to 399.4 and 401.5 eV, respectively, possibly suggesting an electron transfer from N to Ag and thus the development of electron-deficient N species but perhaps more likely the result of final-state effects in the XPS measurements [30]. Moreover, the Ag 3d XPS spectrum of the Ag/NH₂-MSNS catalyst shows that the Ag⁰ 3d_{5/2} and Ag⁰ 3d_{3/2} peaks shift to higher binding energies compared to those of the Ag/MSNS catalyst, an indication of the smaller size of the Ag nanoparticles in the first case [31].

Details regarding the activation of the reactants during the selective hydrogenation of DMO were explored by in-situ FTIR and TPD measurements. The FTIR spectrum of free DMO in Fig. 3a exhibits two peaks associated with the C=O stretching modes at 1805 and 1775 cm⁻¹, one peak corresponding to the CH₃ asymmetric deformation mode at 1472 cm⁻¹, and another two peaks ascribed to C-O vibrations at 1234 and 1184 cm⁻¹ [32]. In the case of DMO adsorbed over the Ag/MSNS and Ag/ NH₂-MSNS catalysts, all the peaks for the C=O and C-O vibrations, especially those related to the C=O moiety, shift to lower frequencies, whereas the feature ascribed to the CH3 group remains unchanged. This strongly suggests that the adsorption of DMO takes place via the C=O groups. Notably, the C=O peaks observed upon adsorption on the Ag/NH2-MSNS catalyst shows additional red-shifts, to 1753 and 1722 cm⁻¹, compared to what is seen on Ag/MSNS (1772 and 1740 cm⁻¹, respectively), a sign of a stronger adsorption of DMO on Ag/NH2-MSNS [17]. The Ag/NH2-MSNS catalyst, with its smaller-sized Ag nanoparticles, possesses more lowcoordinated sites, and this could account for the additional strength seen in the adsorption of DMO.

The TPD data acquired for DMO adsorbed on both catalysts are reported in Fig. 3b. The DMO peak desorption temperature from the Ag/NH₂-MSNS catalyst (747 K) is much higher than that from the Ag/MSNS catalyst (689 K), corroborating the stronger adsorption of DMO on the Ag/NH₂-MSNS catalyst. Moreover, the H₂-TPD profiles in Fig. 3b show similar desorption temperatures for both catalysts but different desorption peak areas in absolute as well

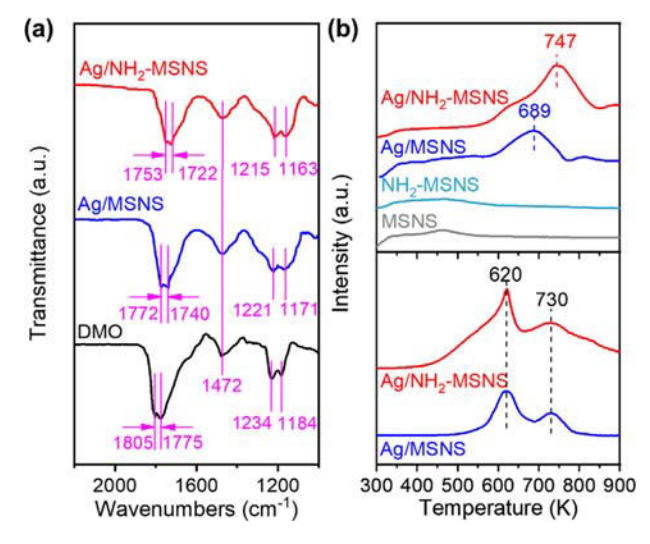


Fig. 3. (a) FTIR spectra of the gas-phase DMO molecule and in situ FTIR spectra of DMO adsorbed on the Ag/MSNS and Ag/NH₂-MSNS catalysts. (b) DMO-TPD data (upper panel) for DMO adsorbed on the Ag/MSNS and Ag/NH₂-MSNS catalysts as well as the supports, and H₂-TPD profiles (bottom) for the Ag/MSNS and Ag/NH₂-MSNS catalysts.

as in relative terms. Considering that equivalent amounts of catalysts were used in both tests, the larger H₂ yield seen with the Ag/NH₂-MSNS catalyst is likely to reflect the smaller Ag particle size (and its corresponding higher metal surface area) in the highly dispersed Ag/NH2-MSNS (Fig. 1f and Table 1). Moreover, the relative higher yield for H₂ in the low-temperature (620 K) peak advocates for a higher reactivity on Ag/NH₂-MSNS (compared to that on Ag/MSNS), as expected from the stronger adsorption already mentioned before. It should be noted that some amino groups are expected to be free and uncoordinated on the surface of NH2-MSNS after Ag+ immobilization, and that those uncoordinated amino group may affect the adsorption and activation of DMO due to the enhanced basicity (as actually demonstrated by the NH₃-TPD profiles in Fig. S6). To exclude this possibility, DMO-TPD measurements were also carried out for MSNS and NH2-MSNS (Fig. 3b). It can be clearly seen that the adsorption of DMO on both pristine and amino-derived supports is negligible compared to that on the catalysts. The catalytic performances of MSNS and NH2-MSNS were also tested: as seen in Table S2, neither of those two samples shows any significant activity for DMO hydrogenation. Thus, it can be concluded that the excess amino group

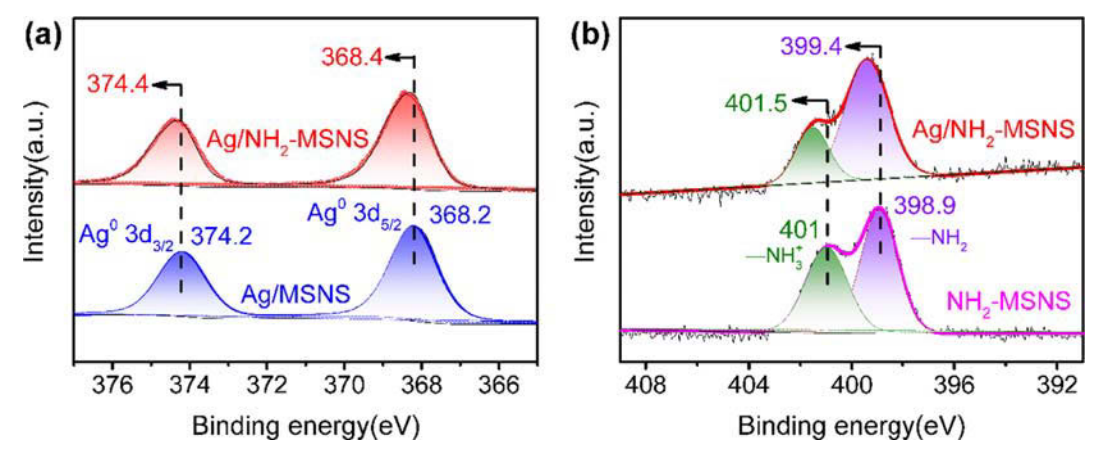


Fig. 2. (a) Ag 3d XPS spectra of Ag/MSNS and Ag/NH₂-MSNS. (b) N 1s XPS spectra of NH₂-MSNS and the supported Ag catalyst.

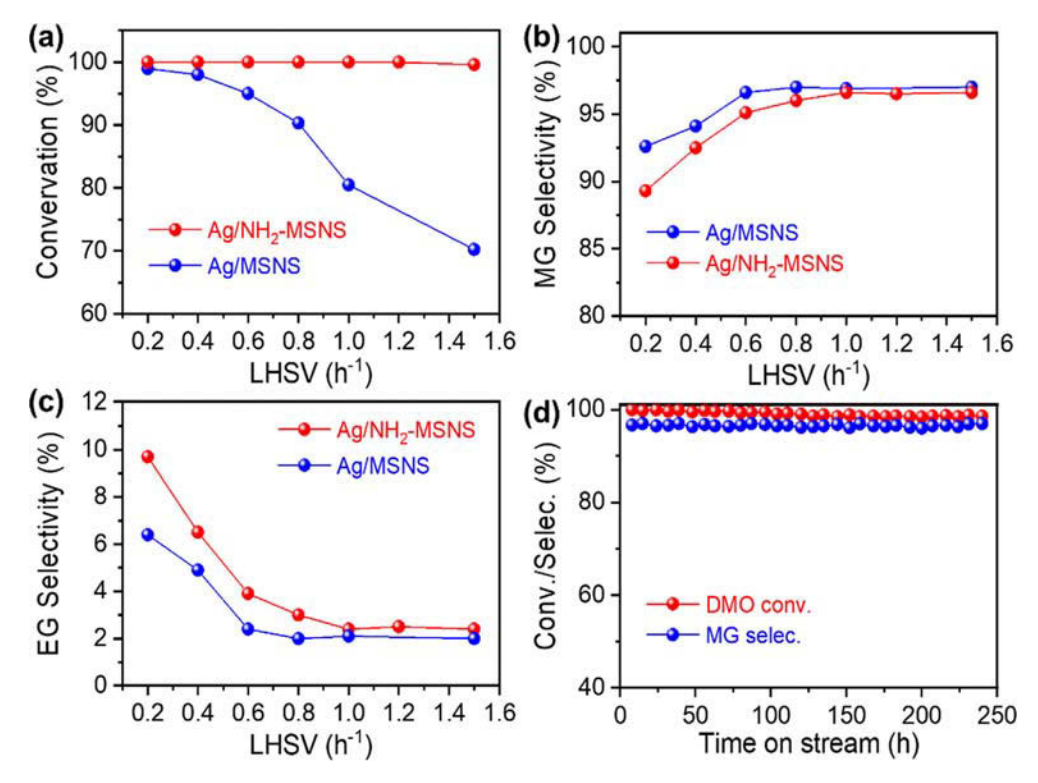


Fig. 4. (a) DMO conversion, (b) MG selectivity and (c) EG selectivity from hydrogenation runs with the Ag/MSNS (blue balls) and Ag/NH₂-MSNS (red balls) catalysts as a function of LHSV. (d) Kinetic data versus time on stream for DMO hydrogenation on the Ag/NH₂-MSNS catalyst under the following reaction condition: T = 493 K, P = 2.0 MPa, $H_2/DMO = 80 \text{ and } LHSV = 1.0 \text{ h}^{-1}$.

Table 2Catalytic performance of various reported catalysts for selective hydrogenation of DMO to MG.

Catalysts	Cu/Ag loading (wt%)	Reaction conditions				Conv. _{DMO} (%)	Selec. _{MG} (%)	$TOF(h^{-1})$	Ref.
		LHSV (h ⁻¹)	Temperature (K)	Pressure (MPa)	H ₂ /DMO (mol/mol)				
Cu-Ni/HMS	2.6	0.2	493	2.5	100	100	86.0	10.6	[33]
Raney Cu	100	2.0	483	2.5	100	70.0	95.0	4.2	[34]
Cu/HAP	20.0	0.4	483	2.5	150	74.0	70.0	14.4	[35]
Cu/AC	20.0	0.2	493	2.5	120	83.0	92.0	17.0	[36]
Cu/SiO ₂	48.5	0.26	493	2.5	200	>90.0	94.0	5.08	[37]
Cu-Ag/Ni-foam	28.0/0.4	0.25	483	2.5	300	96.1	96.1	N/A	[38]
Ag/Ti-KCC-1	10.3	1.75	473	3.0	100	98.0	95.0	16.1	[16]
Ag-B ₂ O ₃ /SiO ₂	10.0	0.2	453	0.5	150	98.9	97.2	N/A	[15]
Ag/AC-N	9.8	0.6	493	3.0	80	95.0	98.0	25.1	[12]
Ag-in/h-CNT	8.1	0.6	493	3.0	80	100	97.0	N/A	[11]
Ag-Ni/SBA-15	5.0	1.0	473	3.0	80	97.6	92.8	106.0	[8,9]
Ag/KCC-1	15.7	1.75	473	3.0	100	100	>90.0	53.2	[14]
Ag/SBA-15	9.3	0.6	473	3.0	80	100	94.0	34.0	[13]
Ag/MCM-41	10.0	0.2	493	2.5	100	96.0	94.0	1.9	[10]
Ag/MSNS	2.5	1.0	493	2.0	80	95.0	96.6	165.1	This wor
Ag/NH ₂ -MSNS	2.9	1.0	493	2.0	80	100	96.6	230.1	This wor

on the support exert no significant effect on the hydrogenation process.

The catalytic performance of the Ag/MSNS and Ag/NH₂-MSNS catalysts was investigated in a comparative way using a fixed-bed flow reactor. The data obtained from runs carried out at 493 K, under 2.0 MPa of pressure, and with a H₂/DMO ratio of 80, are shown in Fig. 4. The Ag/MSNS catalyst shows a gradual decrease in DMO conversion with increasing liquid hourly space velocity (LHSV), from 100% at 0.2 h⁻¹ to 70% at 1.5 h⁻¹, whereas the Ag/NH₂-MSNS catalyst retains a nearly 100% DMO conversion level throughout the whole LHSV range probed here (Fig. 4a). This indicates a higher activity with the Ag/NH₂-MSNS catalyst. That

catalyst does show a slightly lower selectivity to MG and a higher selectivity to ethylene glycol (EG) than the Ag/MSNS catalyst at low LHSVs (Fig. 4b and c), possibly because the overall higher hydrogenation activity favors further conversion of MG to EG as the residence time of the mixture increases. Nevertheless, the difference is small and disappears at higher LHSVs. In the end, the MG yield with the Ag/NH₂-MSNS catalyst is much higher than that with the Ag/MSNS catalyst over most of the LHSV range probed (Fig. S7a). The comparison of the data at LHSV of 1.5 h⁻¹ provided in Fig. S7b further demonstrates the enhanced performance of the Ag/NH₂-MSNS catalyst in comparison to that of the Ag/MSNS catalyst. The calculated turnover frequency (TOF) of DMO conversion

with the Ag/NH₂-MSNS catalyst was estimated to be 230 h⁻¹, much higher than those with the Ag/MSNS catalyst or any other catalysts reported in the literature (Table 2). In particular, the TOF of our Ag/NH₂-MSNS catalyst is above 3 times higher than that of the Ag supported on a novel fibrous nano-silica (KCC-1) material, which displays a similar center-radial pore structures but lower Ag dispersion [14]; the significantly superior hydrogenation activity of the Ag/NH₂-MSNS catalyst compared to that of the Ag/KCC-1 catalyst could be the result of the much higher Ag dispersion and smaller Ag particle size in our catalyst.

Long-term performance tests were performed at a LHSV of 1.0 h⁻¹ to evaluate the stability of our catalyst. Those tests reveal that, with the Ag/NH₂-MSNS catalyst, 100% DMO conversion and 97% selectivity toward MG can be maintained for ca. 250 h (Fig. 4d). The HAADF-STEM image of the used Ag/NH₂-MSNS catalyst acquired after these catalytic tests shown in Fig. S8 demonstrates that the Ag nanoparticles are still well dispersed on the NH₂-MSNS support after this test, with a similar size distribution as that seen in the fresh catalyst. Moreover, a comparative thermogravimetric analysis (TGA) of the fresh versus used catalysts shows negligible coke formation on the used Ag/NH₂-MSNS catalyst (Fig. S9). These results suggest that, by physically confining Ag nanoparticles inside the mesopores, the Ag/NH₂-MSNS catalyst exhibits anti-sintering and anti-coking properties superior to those of other Ag-based catalysts, and thus excellent stability.

4. Conclusions

In summary, here we have introduced a novel synthetic route for the preparation of Ag-based catalysts with high dispersion and small and uniform nanoparticle size. Our strategy has been to start with mesoporous silica nanospheres and to aminate their surfaces via silanization with 3-aminopropyltrimethoxysilane to facilitate the nucleation of Ag nanoparticles, which are deposited afterward. The resulting catalyst was proven to exhibit desirable stability against sintering under catalytic conditions, and excellent catalytic performance. Accordingly, the turnover frequency for the hydrogenation of dimethyl oxalate over this Ag/NH₂-MSNS catalyst reached a value of 230 h⁻¹, with a selectivity toward the desired methyl glycolate product of up to 97% at 100% conversion. This unusually good performance remained stable for at least 250 h. We ascribed the superior performance of our catalyst to the high dispersion and small size of the Ag nanoparticles attained by our synthetic methodology. This is the most efficient catalyst with the least Ag loading reported in the literature so far.

Declaration of Competing Interest

The authors declare that they have no known competing financial interests or personal relationships that could have appeared to influence the work reported in this paper.

Acknowledgements

This work was supported by Ministry of Science and Technology of the People's Republic of China, under the Research Fund for National Key R&D Program of China (2018YFB0604700), and Ministry of Education of the People's Republic of China and State Administration of Foreign Experts Affairs of People's Republic of China, under the Research Fund for the 111 project of China (No. B08021). F.Z. acknowledges funding from the U.S. National Science Foundation (CHE-1953843).

Appendix A. Supplementary material

Supplementary data to this article can be found online at https://doi.org/10.1016/j.jcat.2020.08.018.

References

- [1] Y. Xu, W. Dou, Y. Zhao, G. Huang, X. Ma, Kinetics study for ion-exchange-resin catalyzed hydrolysis of methyl glycolate, Ind. Eng. Chem. Res. 51 (2012) 11653–11658.
- [2] K.Y. Lee, K.H. Bouhadir, D.J. Mooney, Degradation behavior of covalently cross-linked poly (aldehyde guluronate) hydrogels, Macromolecules 33 (2000) 97-101
- [3] Q. Xu, Metal carbonyl cations: generation, characterization and catalytic application, Coord. Chem. Rev. 231 (2002) 83–108.
- [4] T. Turek, D.L. Trimm, The catalytic hydrogenolysis of esters to alcohols, Catal. Rev. 36 (1994) 645–683.
- [5] R. Angamuthu, P. Byers, M. Lutz, A.L. Spek, E. Bouwman, Electrocatalytic CO₂ conversion to oxalate by a copper complex, Science 327 (2010) 313–315.
- [6] H. Yue, Y. Zhao, X. Ma, J. Gong, Ethylene glycol: properties, synthesis, and applications, Chem. Soc. Rev. 41 (2012) 4218–4244.
- [7] Y. Song, J. Zhang, J. Lv, Y. Zhao, X. Ma, Hydrogenation of dimethyl oxalate over copper-based catalysts: acid-base properties and reaction paths, Ind. Eng. Chem. Res. 54 (2015) 9699–9707.
- [8] J. Zhou, X. Duan, L. Ye, J. Zheng, M.M.J. Li, S.C.E. Tsang, Y. Yuan, Enhanced chemoselective hydrogenation of dimethyl oxalate to methyl glycolate over bimetallic Ag-Ni/SBA-15 catalysts, Appl. Catal. A 505 (2015) 344–353.
- [9] M.M.L. Li, L. Ye, J. Zheng, H. Fang, A. Kroner, Y. Yuan, S.C.E. Tsang, Surfactant-free nickel-silver core@shell nanoparticles in mesoporous SBA-15 for chemoselective hydrogenation of dimethyl oxalate, Chem. Commun. 52 (2016) 2569–2572.
- [10] A. Yin, C. Wen, W. Dai, K. Fan, Ag/MCM-41 as a highly efficient mesostructured catalyst for the chemoselective synthesis of methyl glycolate and ethylene glycol, Appl. Catal. B 108–109 (2011) 90–99.
- [11] J. Zheng, X. Duan, H. Lin, Z. Gu, H. Fang, J. Li, Y. Yuan, Silver nanoparticles confined in carbon nanotubes: on the understanding of the confinement effect and promotional catalysis for the selective hydrogenation of dimethyl oxalate, Nanoscale 8 (2016) 5959–5967.
- [12] M. Hu, Y. Yan, X. Duan, L. Ye, J. Zhou, H. Lin, Y. Yuan, Effective anchoring of silver nanoparticles onto N-doped carbon with enhanced catalytic performance for the hydrogenation of dimethyl oxalate to methyl glycolate, Catal. Commun. 100 (2017) 148–152.
- [13] J. Zheng, H. Lin, X. Zheng, X. Duan, Y. Yuan, Highly efficient mesostructured Ag/ SBA-15 catalysts for the chemoselective synthesis of methyl glycolate by dimethyl oxalate hydrogenation, Catal. Commun. 40 (2013) 129–133.
- [14] M. Ouyang, Y. Wang, J. Zhang, Y. Zhao, S. Wang, X. Ma, Three dimensional Ag/ KCC-1 catalyst with a hierarchical fibrous framework for the hydrogenation of dimethyl oxalate, RSC Adv. 6 (2016) 12788–12791.
- [15] H. Chen, J. Tan, J. Cui, X. Yang, H. Zheng, Y. Zhu, Y. Li, Promoting effect of boron oxide on Ag/SiO₂ catalyst for the hydrogenation of dimethyl oxalate to methyl glycolate, Mol. Catal. 433 (2017) 346–353.
- [16] M. Ouyang, J. Wang, B. Peng, Y. Zhao, S. Wang, X. Ma, Effect of Ti on Ag catalyst supported on spherical fibrous silica for partial hydrogenation of dimethyl oxalate, Appl. Surf. Sci. 466 (2019) 592–600.
- [17] L. Fleming, Molecular Orbitals and Organic Chemical Reactions, John Wiley & Sons Ltd, 2009, pp. 59–69.
- [18] D. Shen, J. Yang, X. Li, L. Zhou, R. Zhang, W. Li, L. Chen, R. Wang, F. Zhang, D. Zhao, Biphase stratification approach to three-dimensional dendritic biodegradable mesoporous silica nanospheres, Nano Lett. 14 (2014) 923–932.
- [19] X. Liu, A. Wang, X. Yang, T. Zhang, C.Y. Mou, D.S. Su, J. Li, Synthesis of thermally stable and highly active bimetallic Au-Ag nanoparticles on inert supports, Chem. Mater. 21 (2009) 410-418.
- [20] C.J.G. Van Der Grift, A.F.H. Wielers, B.P.J. Jogh, J. Van Beunum, M. De Boer, M. Versluijs-Helder, J.W. Geus, Effect of the reduction treatment on the structure and reactivity of silica-supported copper particles, J. Catal. 131 (1991) 178–189.
- [21] M. Boudart, Turnover rates in heterogeneous catalysis, Chem. Rev. 95 (1995) 661–666.
- [22] J. Tan, J. Cui, G. Ding, S.D. Tian, Y. Li, Efficient aqueous hydrogenation of levulinic acid to γ-valerolactone over highly active and stable ruthenium catalyst, Catal. Sci. Technol. 6 (2016) 1469–1475.
- [23] D.K. Shen, L. Chen, J.P. Yang, R.Y. Zhang, Y. Wei, X.M. Li, W. Li, Z.K. Sun, H.W. Zhu, A.M. Abdullah, A. Al-Enizi, A.A. Elzatahry, F. Zhang, D.Y. Zhao, Ultradispersed palladium nanoparticles in three-dimensional dendritic mesoporous silica nanospheres: toward active and stable heterogeneous catalysts, Acs Appl. Mater. Inter. 7 (2015) 17450–17459.
- [24] A. Yin, X. Guo, W. Dai, K. Fan, High activity and selectivity of Ag/SiO₂ catalyst for hydrogenation of dimethyl oxalate, Chem. Commun. 46 (2010) 4348–4350.
- [25] Y. Wang, Y. Zheng, C.Z. Huang, Y. Xia, Synthesis of Ag nanocubes 18–32 nm in edge length: the effects of polyol on reduction kinetics, size control, and reproducibility, J. Am. Chem. Soc. 135 (2013) 1941–1951.
- [26] N.G. Bastús, F. Merkoçi, J. Piella, V. Puntes, Synthesis of highly monodisperse citrate-stabilized silver nanoparticles of up to 200 nm: kinetic control and catalytic properties, Chem. Mater. 26 (2014) 2836–2846.

- [27] S.H. Im, Y.T. Lee, B. Wiley, Y. Xia, Large-scale synthesis of silver nanocubes: the role of HCl in promoting cube perfection and monodispersity, Angew. Chem. Int. Ed. 44 (2005) 2154–2157.
- [28] J. Zhao, F. Gao, S.P. Pujari, H. Zuilhof, A.V. Teplyakov, Universal calibration of computationally predicted N1s binding energies for interpretation of XPS experimental measurements, Langmuir 33 (2017) 10792–10799.
- [29] T. Yoshida, S. Sawada, X-ray photoelectron spectroscopy of EDTA, Bull. Chem. Soc. Jpn. 47 (1974) 50–53.
- [30] W.F. Egelhoff Jr, Core-level binding-energy shifts at surfaces and in solids, Surf. Sci. Rep. 6 (1987) 253-415.
 [31] I. Aruna, B.R. Mehta, L.K. Malhotra, S.M. Shivaprasad, Size dependence of core
- [31] I. Aruna, B.R. Mehta, L.K. Malhotra, S.M. Shivaprasad, Size dependence of core and valence binding energies in Pd nanoparticles: interplay of quantum confinement and coordination reduction, J. Appl. Phys. 104 (2008) 064308.
- [32] G.Q. Cui, X.Y. Meng, X. Zhang, W.L. Wang, S.L. Xu, Y.C. Ye, K.J. Tang, W.M. Wang, J.H. Zhu, M. Wei, D.G. Evans, X. Duan, Low-temperature hydrogenation of dimethyl oxalate to ethylene glycol via ternary synergistic catalysis of Cu and acid-base sites, Appl. Catal. B 248 (2019) 394–404.
 [33] A.Y. Yin, C. Wen, X.Y. Guo, W.L. Dai, K.N. Fan, Influence of Ni species on the
- [33] A.Y. Yin, C. Wen, X.Y. Guo, W.L. Dai, K.N. Fan, Influence of Ni species on the structural evolution of Cu/SiO₂ catalyst for the chemoselective hydrogenation of dimethyl oxalate, J. Catal. 280 (2011) 77–88.

- [34] X.P. Kong, C.L. Ma, J. Zhang, J.Q. Sun, J.G. Chen, K.F. Liu, Effect of leaching temperature on structure and performance of Raney Cu catalysts for hydrogenation of dimethyl oxalate, Appl. Catal. A 509 (2016) 153–160.
- [35] C. Wen, Y.Y. Cui, X. Chen, B.N. Zong, W.L. Dai, Reaction temperature controlled selective hydrogenation of dimethyl oxalate to methyl glycolate and ethylene glycol over copper-hydroxyapatite catalysts, Appl. Catal. B 162 (2015) 483– 493.
- [36] Y.Y. Cui, B. Wang, C. Wen, X. Chen, W.L. Dai, Investigation of activated-carbonsupported copper catalysts with unique catalytic performance in the hydrogenation of dimethyl oxalate to methyl glycolate, Chemcatchem 8 (2016) 527–531.
- [37] M. Abbas, Z. Chen, J. Zhang, J.G. Chen, Highly dispersed, ultra-small and noble metal-free Cu nanodots supported on porous SiO₂ and their excellent catalytic hydrogenation of dimethyl oxalate to methyl glycolate, New J. Chem. 42 (2018) 10290–10299.
- [38] Y. Chen, L. Han, J. Zhu, P. Chen, S. Fan, G. Zhao, Y. Liu, Y. Lu, High-performance Ag-CuO_x nanocomposite catalyst galvanically deposited onto a Ni-foam for gas-phase dimethyl oxalate hydrogenation to methyl glycolate, Catal. Commun. 96 (2017) 58–62.